2 Background

This chapter considers important background information which are needed to prepare the development, testing and analysis as well as the application of the seismic source location algorithm designed in this work. It starts with a section about earthquakes and their different seismic sources and continues with a section that describes how to mathematically express and hence model those sources in homogeneous and isotropic media. After the basis for the modeling of synthetic data is build a section about multicomponent seismology follows. It considers different approaches and the estimation of polarization information of three-component data and discusses applicability and pitfalls. Once estimation techniques and the reliability of polarization information are discussed this chapter closes with a section about kinematic ray tracing and the theoretical background for its implementation in the presented location algorithm.

2.1 Earthquakes

The occurrence of earthquakes has been observed for thousands of years. In general, an earthquake is defined as a sudden movement or shaking of the Earth's crust resulting from abrupt release of accumulated stress in the Earth (Sheriff, 2002). Earthquakes mainly occur in the outer 30 km of the Earth, where rocks tend to break (brittle failure of rock) rather than deforming ductile under stress. Nevertheless, earthquakes commonly assoschiated with phase alterations can be observed at depth as great as 700 km in subduction zones. Naturally induced earthquakes as shown in Figure 2.1 are mainly associated with tectonic activity, volcanoes, rockfalls, and landslides. On the other hand, its also known that human activity (such as explosions, mining, production from hydrocarbon reservoirs or reservoir stimulation) causes earthquakes.

Brittle failure of rocks can be caused in different ways. The governing failure mechanisms are associated with tensile failure and shear failure and can be de-
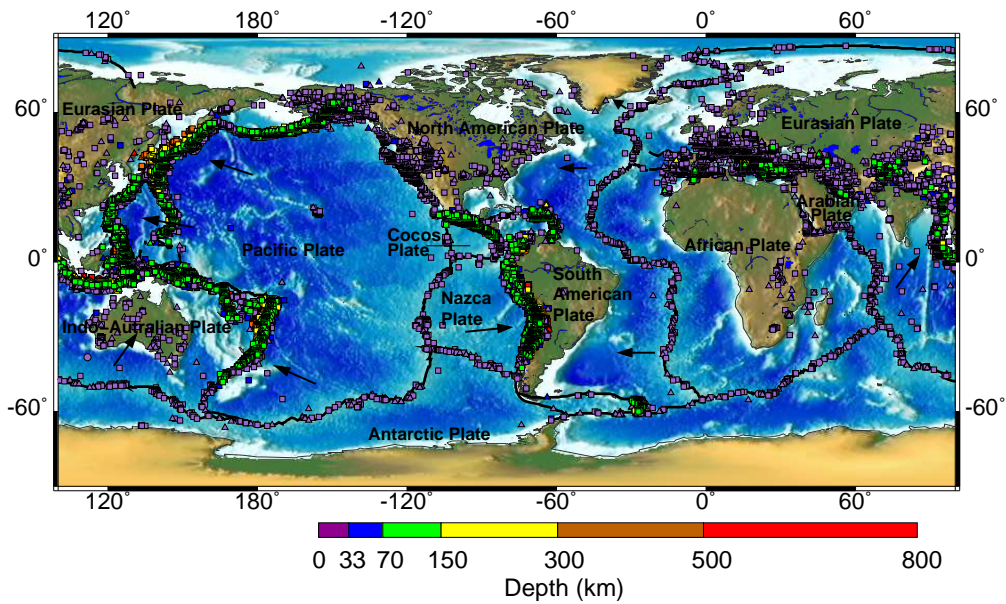
Figure 2.1: Distribution of global seismicity from 2005 to 2007. Events were loaded from several catalogs (indicated by different markers) and plotted with the IRIS online mapping tool (http://www.iris.edu/SeismiQuery/events.htm). The depths of the events are color-coded.

scribed by mapping stress states in a Mohr-Coulomb diagram as shown in Figure 2.2. The principle stresses σ_1, σ_2 and σ_3 can be used to describe the stress state, with σ_1 being the maximum principle stress and σ_3 the minimum principle stress (Scholz, 2002). Compressive stresses are defined as positive.

Tensile failure occurs when tensile stress exceeds the tensile strength T of the rock (see the magenta solid line in Figure 2.2). The tensile failure criterion can be formulated relating the smallest component of principal stress to the tensile strength T of the rock:

$$\sigma_3 = -T. \tag{2.1}$$

The shear failure of rocks is described by the Mohr-Coulomb criterion:

$$\tau = \tau_0 + \mu \cdot \sigma_n, \tag{2.2}$$

where τ and σ_n are the shear and normal stresses resolved on any plane within the material. τ_0 represents a term of cohesion. The parameter μ is called the coefficient of internal friction and is often expressed as $\tan\phi$ with ϕ being the angle of internal friction. Shear failure occurs when the shear stress associated with the stress state intersects the Mohr-Coulomb envelope (see green solid line in Figure 2.2).

As shown by Figure 2.2 the stress state can be mapped drawing the Mohr-Coulomb's circle. Any circle of this kind is characterized by a radius $(\sigma_1 - \sigma_3)/2$
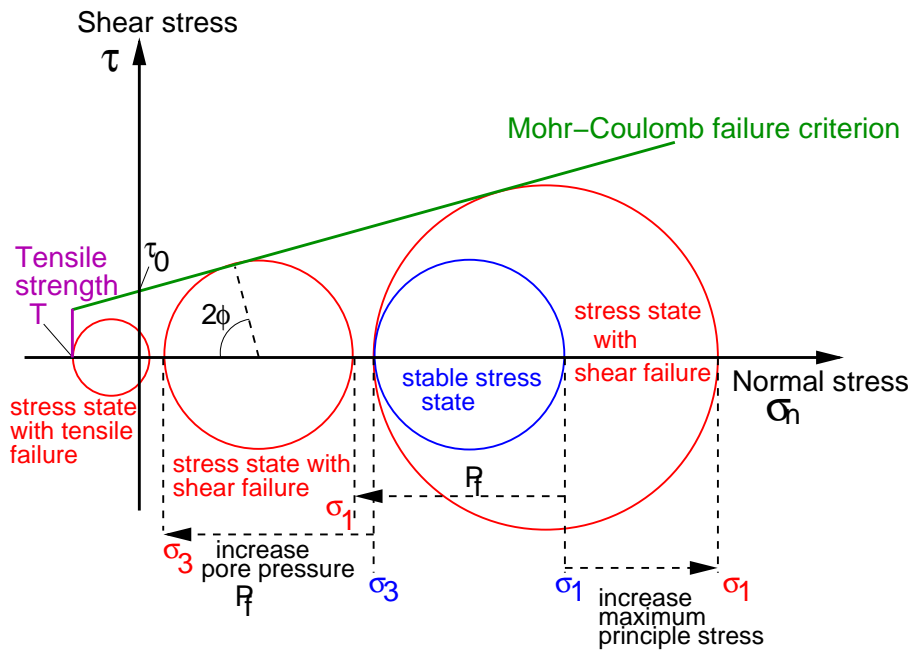
Figure 2.2: Failure criteria related to the stress state of the rock.

and a center $(\sigma_1 - \sigma_3)/2$ located on the σ_n axis. The rock is in a stable stress state as long as the Mohr-Coulomb circle does neither exceed tensile strength nor the shear strengths as shown by the blue Mohr-Coulomb circle in Figure 2.2.

There are three major ways to change the stress state in order to cause failure. One is associated with compressional motion which increases the maximum principle stress σ_1 and leaves the minimum principle stress σ_3 constant. The stress within the material, and hence the radius of the Mohr-Coulomb circle (see Figure 2.2), can increase only until the failure criterion is tangent to the circle. Shear failure follows. This scenario can be observed at convergent plate boundaries where earthquakes occur at several depths ranging from the very near surface to several hundred kilometers (see Figure 2.1) because the temperatures of the subducting plate permits brittle failure down to at least 300 km (e.g., Carminati et al.). Deeper earthquakes are generally related to other mechanisms, such as e.g., dehydration embrittlement, faulting induced by a phase alteration or adiabatic shear instability (see Green II, 2003). Furthermore, the largest earthquakes occur at convergent plate boundaries, e.g., some events on subduction zones in Alaska and Chile have exceeded magnitude 9.

On the other hand, the radius of the Mohr-Coulomb circle can also be increased by decreasing the minimum principle stress σ_3 while leaving the maximum principle stress σ_1 constant. This change is associated with crustal extension as at spreading ridges, or similar extensional boundaries like rifts or grabens. Earthquakes in extensional environments are relatively shallow and have usually magnitudes

smaller than 8 (see Figure 2.1).

Both, compressional as well as extensional stress states can be locally observed at strike-slip faults, which is often called transpression or transtension (Zoback, 1991). Earthquakes are relatively shallow (as deep as 25 km) and their mechanisms indicate strike-slip motion. The magnitudes are not as large as at convergent plate boundaries but can still reach magnitudes of 8.5. One if the most prominent example of strike-slip faults is the San Andreas Fault in California, which separates the Pacific from the North American plate.

The third possibility to change the stress state is caused by changes in pore/fluid pressure P_f. The increase of fluid pressure changes the effective normal stress σ_n^{eff} which is defined as the difference between the normal stress σ_n and the pore pressure P_f (see Figure 2.3) , i.e.

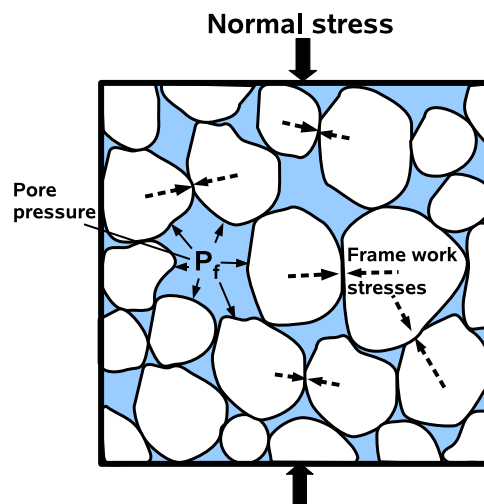$$\sigma_n^{eff} = \sigma_n - P_f. \tag{2.3}$$

Figure 2.3: Schematic representation of the interaction of frame work stresses and pore pressure P_f.

The increasing pore pressure decreases the effective normal stress by the same order of magnitude which causes a shift of the stress circle towards the failure envelope (Figure 2.2). If the stress circle is tangent to the Mohr-Coulomb envelope shear failure will occur and if the stress circle exceeds the tensile strength T tensile failure can be observed. Those fluid induced earthquakes are often observed in relation with water-level-changes in lakes, in mines and in water dam reservoirs, or even with heavy rainfalls (Talwani and Acree, 1985; Costain and Bollinger, 1991; Hainzl et al., 2006). At the same time, fluid induced earthquakes can also be man-made, which means they can be caused by fluid injections such as hydraulic stimulations/fracturing of rocks (see, e.g., Albright and Pearson, 1980; Shapiro et

al., 1997; Zoback and Harjes, 1997; Shapiro et al., 1999; Shapiro, 2000; Rutledge and Phillips, 2003; Rutledge et al., 2004).

All these different earthquake sources cause seismic waves that propagate through the earth and can be recorded with geophones. The seismic wavefield observed at different geophone locations will differ in many ways depending on the medium the waves traveled through and on local conditions at the receiver and the source. In this work the whole wavefield will be analyzed but only direct body waves will be used to invert the wavefield for the seismic source location. For this reason the next section will describe which wavefield can be expected from direct body waves radiated from different seismic sources.

2.2 Seismic sources

The seismic wavefield recorded at a three component receiver depends on the medium parameters, the distance between source and receiver and the source type itself. In this thesis a general approach that evaluates the seismic moment tensor components is used to describe the far field displacement in homogeneous isotropic media. The moment tensor $\mathbf{M}$ is defined as

$$\mathbf{M} = \begin{bmatrix} M_{11} & M_{12} & M_{13} \\ M_{21} & M_{22} & M_{23} \\ M_{31} & M_{32} & M_{33} \end{bmatrix},$$ (2.4)

where each entry M_{kl} describes a pair of bi-directional forces pointing in the direction k and being separated in the direction l as shown in Figure 2.4. With this set of point dipoles and single couples any source type can be described, e.g. an explosion source can be represented by a moment tensor with non-zero elements only along the main diagonal of $\mathbf{M}$.

Following the notation of Strelitz (1978), the recorded far field displacement field $\mathbf{u}$ for a point source can be written using the first derivative of the Green's function $\mathbf{G}'$ and the second order moment tensor $\mathbf{M}$:

$$\mathbf{u} = \mathbf{G}'\mathbf{M} = c\mathbf{F}\mathbf{M}$$ (2.5)

with

$$c = \frac{1}{4\pi\rho v^3 R}$$ (2.6)

R represents the distance from the source to the receiver and v denotes the wave velocity, respectively. $\mathbf{F}$ is called the excitation matrix and describes P-, SV- and SH- body waves. For a homogeneous, isotropic, and infinite medium it has the following form:
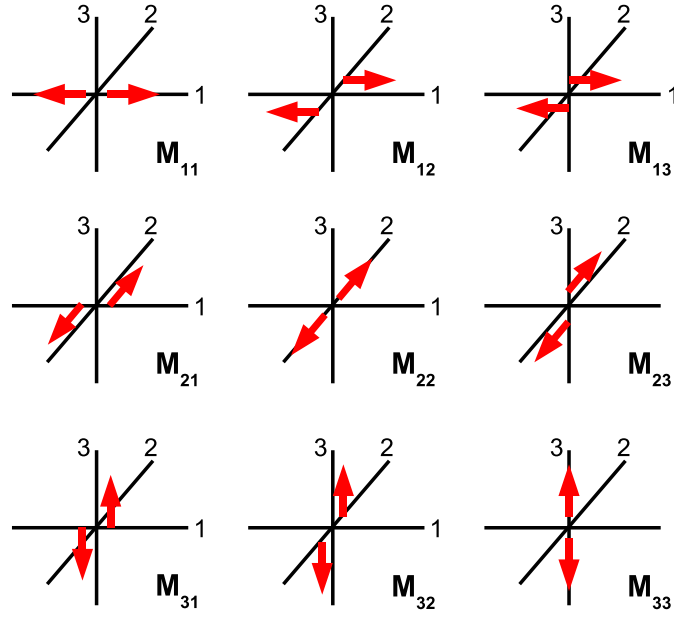
Figure 2.4: The components of the moment tensor represent nine different force couples.

$$F_P = \begin{pmatrix} \sin^2\phi\cos^2\varphi & \frac{1}{2}\sin^2\phi\sin 2\varphi & \frac{1}{2}\sin 2\phi\cos\varphi \\ \frac{1}{2}\sin^2\phi\sin 2\varphi & \sin^2\phi\sin^2\varphi & \frac{1}{2}\sin 2\phi\sin\varphi \\ \frac{1}{2}\sin 2\phi\cos\varphi & \frac{1}{2}\sin 2\phi sin\varphi & \cos^2\phi \end{pmatrix}, \qquad (2.7)$$

$$F_{SV} = \begin{pmatrix} \frac{1}{2}\sin 2\phi\cos^2\varphi & \frac{1}{4}\sin 2\phi\sin 2\varphi & \cos^2\phi\cos\varphi \\ \frac{1}{4}\sin 2\phi\sin 2\varphi & \frac{1}{2}\sin 2\phi\sin^2\varphi & \cos^2\phi\sin\varphi \\ -\sin^2\phi\cos\varphi & -\sin^2\phi\sin\varphi & -\frac{1}{2}\sin 2\phi \end{pmatrix}, \qquad (2.8)$$

$$F_{SH} = \begin{pmatrix} -\frac{1}{2}\sin\phi\sin 2\varphi & -\sin\phi\sin^2\varphi & -\cos\phi\sin\varphi \\ -\sin\phi\cos^2\varphi & \frac{1}{2}\sin\phi\sin 2\varphi & \cos\phi\cos\varphi \\ 0 & 0 & 0 \end{pmatrix} \qquad (2.9)$$

with ϕ being the take-off angle and φ the azimuth angle.

For simplification, here only sources that do not change the angular momentum are considered. Hence the condition $M_{kl} = M_{lk}$ should be fulfilled which makes the momentum tensor symmetric. A symmetric moment tensor only holds six independent entries and a vector notation can be introduced to replace matrix notations:

$$
\begin{aligned}
m_1 &= M_{11} & f_1 &= F_{11} \\
m_2 &= M_{12} = M_{21} & f_2 &= F_{12} + F_{21} \\
m_3 &= M_{22} & f_3 &= F_{22} \\
m_4 &= M_{13} = M_{31} & f_4 &= F_{13} + F_{31} \\
m_5 &= M_{23} = M_{32} & f_5 &= F_{23} + F_{32} \\
m_6 &= M_{33} & f_6 &= F_{33}
\end{aligned}
\tag{2.10}
$$

Therefore, any displacement field u_i can be expressed by the sum of these independent entries

$$
u(i) = \sum_{j=1}^{6} (c(i) f_j(i) m_j,
\tag{2.11}
$$

where i represents the observation components.

The displacement of an explosion source is defined by an equivalent force system ($m_1 = m_3 = m_6 \neq 0$) that consists of three perpendicular dipoles of equal strength, which corresponds to the isotropic part of the moment tensor. The P-wave radiation pattern is spherical and there is no direct S-wave radiation observable in the far field. Hence, the radiation pattern of an explosion source can be written as:

$$
\begin{aligned}
u_P &= \frac{1}{4\pi\rho v^3 R}(m_1 f_1(P) + m_3 f_3(P) + m_6 f_6(P)) \\
&= \frac{1}{4\pi\rho v^3 R} m_1(\sin^2\phi\cos^2\varphi + \sin^2\phi\sin^2\varphi + \cos^2\phi) \\
&= \frac{1}{4\pi\rho v^3 R} m_1(\sin^2\phi(\cos^2\varphi + \sin^2\varphi) + \cos^2\phi) \\
&= \frac{1}{4\pi\rho v^3 R} m_1
\end{aligned}
\tag{2.12}
$$

In order to simulate a seismogram it is necessary to introduce a source time function or seismic moment rate function $K'(t)$ which reflects the pulse radiated from the source. The pulse propagates away from the source with the velocity v and arrives at a receiver at distance r at time $t - \frac{r}{v}$ with the displacement

$$
u_P = \frac{1}{4\pi\rho v^3 R} \cdot K'\left(t - \frac{r}{v}\right).
\tag{2.13}
$$

Using the same procedure, seismograms of double couple sources can be expressed selecting a force system of the moment tensor. For example consider shear failure in the x-y(1-2) plane or y-z(2-3) plane with relative displacement

in x-direction or z-direction. The moment tensor of such a source has only two non-zero components M_{13} and M_{31}. Hence the displacement for such a source can be described in the following way:

$$
\begin{aligned}
u_P &= \frac{1}{4\pi\rho v^3 R}(m_4 f_4(P)) \\
&= \frac{1}{4\pi\rho v^3 R}m_4(\frac{1}{2}\sin 2\phi \cos\varphi + \frac{1}{2}\sin 2\phi \cos\varphi) \\
&= \frac{1}{4\pi\rho v^3 R}m_4(\sin 2\phi \cos\varphi)
\end{aligned}
$$

and using a source time function

$$
u_P = \frac{\sin 2\phi \cos\varphi}{4\pi\rho v^3 R}\cdot K'\left(t - \frac{r}{v}\right), \tag{2.14}
$$

$$
\begin{aligned}
u_{SV} &= \frac{1}{4\pi\rho v^3 R}(m_4 f_4(SV)) \\
&= \frac{1}{4\pi\rho v^3 R}m_4(\frac{1}{2}\cos^2\phi \cos\varphi - \sin^2\phi \cos\varphi) \\
&= \frac{1}{4\pi\rho v^3 R}m_4 \cos\varphi(\frac{1}{2} + \frac{1}{2}\cos 2\phi - \frac{1}{2} + \frac{1}{2}\cos 2\phi)
\end{aligned}
$$

and using a source time function

$$
u_{SV} = \frac{\cos\varphi \cos 2\phi}{4\pi\rho v^3 R}\cdot K'\left(t - \frac{r}{v}\right) \tag{2.15}
$$

$$
\begin{aligned}
u_{SH} &= \frac{1}{4\pi\rho v^3 R}(m_4 f_4(SH)) \\
&= \frac{1}{4\pi\rho v^3 R}m_4(-\cos\phi \sin\varphi + 0)
\end{aligned}
$$

and using again a source time function

$$
u_{SH} = \frac{-\cos\phi \sin\varphi}{4\pi\rho v^3 R}\cdot K'\left(t - \frac{r}{v}\right). \tag{2.16}
$$

The radiation pattern for P-, SH- and SV-waves obtained from these equations is shown in Figure 2.5. The obtained P-wave particle motion is parallel to the direction of propagation whereas the S-wave particle motion is perpendicular to the
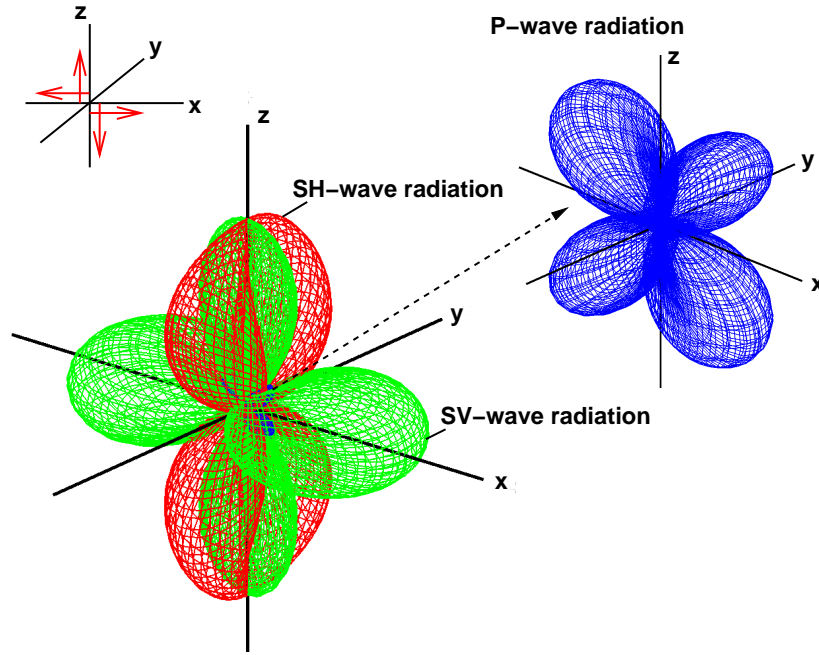
Figure 2.5: Radiation pattern of a double couple in the x-z-plane separated into its components for the P-wave (blue), SH-wave(red) and SV-wave (green), respectively.

direction of propagation. The far field amplitudes of both, P- and S-waves decay proportional to the distance R. Furthermore it can be seen, that the amplitude of the S-wave is $\left(\frac{v_p}{v_s}\right)^3$ times larger then the P-wave amplitude. Assuming a constant Poisson ratio of 1.73 the S-wave amplitude is 5 times larger than the P-wave amplitude.

In this work synthetic seismograms for explosion sources were modeled with equation (2.13) and for double couple sources using the equations (2.14), (2.15) and (2.16). The displacement field can be transformed from spherical coordinates into Cartesian coordinates using the following transformation matrix

$$\begin{pmatrix} \sin\phi\cos\varphi & \cos\phi\cos\varphi & -\sin\varphi \\ \sin\phi\sin\varphi & \cos\phi\sin\varphi & \cos\varphi \\ \cos\phi & -\sin\phi & 0 \end{pmatrix} \begin{pmatrix} u_P \\ u_{SV} \\ u_{SH} \end{pmatrix} = \begin{pmatrix} u_x \\ u_y \\ u_z \end{pmatrix} \qquad (2.17)$$

There are may different ways to describe a source time function $K'(t)$. For the considerations in this work the shape of the source time function does not play a key role. A Küpper-type wavelet as described in Fuchs and Müller (1971) was chosen to represent the seismic moment rate function.

2.3 Multi-component seismology

Multi-component seismology comprises the investigation of the vertical component as well as the horizontal components of ground motion. Thus the corresponding seismic record is a vector quantity that contains significantly more information on the propagating wavefield. For isotropic media, the particle motion of a compressional wave is oriented in the direction of propagation as shown in Figure 2.6 (a). Consequently the particle motion is parallel to the ray path. In contrast, shear waves are associated with particle motion perpendicular to the direction of propagation (see Figure 2.6 (b)). The vector of the particle motion lies within a plane perpendicular to the propagation direction (ray) and its orientation depends on the type or orientation of the source (Tatham and McCormack, 1991). Furthermore, Rayleigh wave particle motion in isotropic media is characterized by a 90 degree phase shift between the vertical and the in-line components which results in elliptical particle motion (see Figure 2.6 (c)). The particle motion of Love waves is horizontal and linear (like an SH-wave, see Figure 2.6 (d)) with an azimuth transverse to the propagation direction (Vidale, 1986). However, due to its late arrival as well as its dispersive character it is unlikely that a Love wave is interpret as an S-wave.
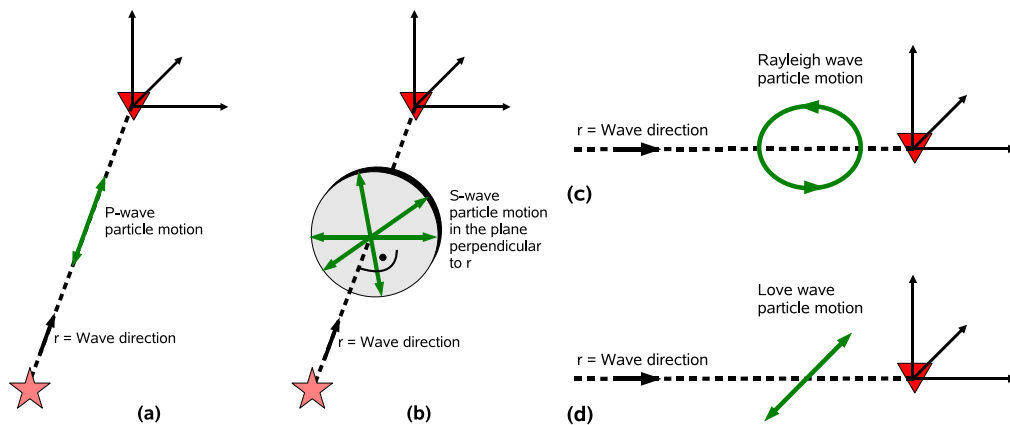

Figure 2.6: Geometry of propagation direction and polarization directions for P-waves (a), S-waves (b), Rayleigh waves (c) and Love waves (d).

Hence the evaluation of particle motion recorded with three-component sensors enables the discrimination between surface waves, compressional waves and shear waves. This can be achieved by comparing the direction of wave propagation with the direction of particle motion. The evaluation process that quantitatively describes the particle motion of a recorded wavefield is called polarization analysis. The success of polarization analysis depends on the accuracy with which the three-component wavefield is recorded. It must represent the true vector wavefield and must not be distorted during acquisition or preprocessing. Acquisition related problems occur when the sensor response or the coupling is not the same for all three components (see section 3.5 in this thesis as well as Hendrick and

Hearn (1999)). The dynamic range of the three-component recording system must also be sufficient to record "true" amplitudes without any clipping or distortion. Preprocessing problems can occur during digitalization. Component timing and amplitude equalization must be identical on all components. As stated by Hendrick and Hearn (1999) it is generally not advisable to rectify sensitivity/coupling problems (e.g., by relative component scaling) unless independent calibration information is available. They point out a guiding rule that any scalar applied to the data must be identical on all components. This makes data independent scaling preferable over data dependent scaling methods like AGC applications. Special care must be taken when frequency and/or velocity filtering is applied since noise removal can also modify the underlying signal.

In general polarization analysis is a vector processing technique that can be performed graphically - via visual evaluation of a so called hodogram, or mathematically obtaining measurements that express the polarization behavior observed in a particle motion hodogram. The graphical approach becomes impractical for data sets as large as it typically is for seismic exploration and production. Many different algorithms to evaluate particle motion in an automated way were proposed in the last 50 years (see e.g., Flinn, 1965; Park et al., 1987; Jurkevics, 1988; Bataille and Chiu, 1991; Li and Crampin, 1991; Franco and Musacchio, 2001). Apart from Li and Crampin (1991) all proposed automated algorithms consider the wavefield in a given time interval.

The estimates typically yield three parameters which express the polarization behavior observed in a particle motion hodogram: (1) rectilinearity, (2) dip and (3) azimuth. Hearn and Hendrick (1999) give a comparison of single-trace time-domain polarization analysis algorithms. They concluded that the investigated approaches for polarization estimates yield remarkably similar results but differed a lot in computation times.

In this work, the analysis of the polarization behavior over time intervals was adapted from Jurkevics (1988). Considering a time interval of three-component data u_x, u_y and u_z containing N time samples auto- and cross-variances can be obtained from:

$$C_{ij} = \left[\frac{1}{N} \sum_{s=1}^{N} u_i(s)u_j(s) \right] \tag{2.18}$$

where i and j represent the component indices x, y, z and s is the index variable for a time sample. The 3×3 covariance matrix

$$\mathbf{C} = \begin{pmatrix} C_{xx} & C_{xy} & C_{xz} \\ C_{xy} & C_{yy} & C_{yz} \\ C_{xz} & C_{yz} & C_{zz} \end{pmatrix} \tag{2.19}$$

is real and symmetric and represents a polarization ellipsoid with best fit to the data. The principal axis of this ellipsoid can be obtained by solving $\mathbf{C}$ for its eigenvalues $\lambda_1 \geq \lambda_2 \geq \lambda_3$ and eigenvectors p_1, p_2, p_3:

$$(\mathbf{C} - \lambda\mathbf{I})\mathbf{p} = 0 \qquad (2.20)$$

where $\mathbf{I}$ is the identity matrix.

The parameter called rectilinearity L, sometimes also called linearity, relates the magnitudes of the intermediate and the smallest eigenvalue to the largest eigenvalue

$$L = 1 - \left(\frac{\lambda_2 + \lambda_3}{2\lambda_1}\right), \qquad (2.21)$$

and is a measure of how linear the wavefield is polarized. It yields values between zero and one. For a perfectly linearly polarized signal the largest eigenvalue λ_1 of the covariance matrix is much larger than the two other eigenvalues. Hence the rectilinearity L will have values close to one. For signals with elliptical polarizations the magnitudes of the eigenvalues will be much more similar and hence the rectilinearity decreases.
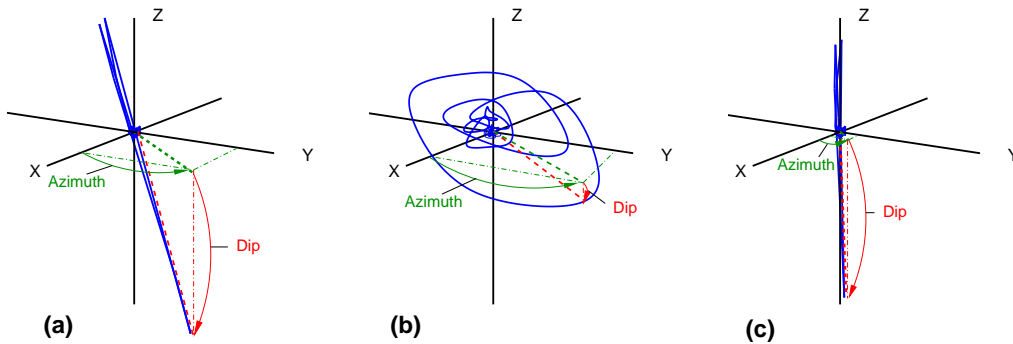

Figure 2.7: Polarization parameter sketch. Polarization information are decribed by rectininearity, dip and azimuth. The wave in (a) is characterized by high rectilinearity, medium dip and hence a reliable azimuth estimate. In (b) the rectilinearity is low and dip and azimuth are difficult to estimate. In (c) the rectilinearity is high. The energy is mainly observed at the vertical component which results in a reliable dip estimate but an unreliable azimuth estimate.

The rectilinearity is a very reliable measure to distinguish between body waves and Rayleigh waves (at least in isotropic media). In Figure 2.7 (a) and (c) waves with high rectilinearity as observed for body waves are shown, whereas a wave with low rectilinearity as shown in (b) is rather associated with a elliptically polarized surface waves.

The other two polarization parameters (dip and azimuth) describe the orientation of the largest eigenvector $p_1 = (p_1(x), p_1(y), p_1(z))$ (see Figure 2.7). The dip can be calculated by

$$\phi = \arctan\left(\frac{p_1(z)}{\sqrt{p_1(x)^2 + p_1(y)^2}}\right). \tag{2.22}$$

It is zero for horizontal polarization and is defined positive in positive z-direction. It is clear that the estimation of dip is only meaningful for linear polarized waves and will not give reliable information when applied to Rayleigh wave recordings.

The azimuth is specified as

$$\theta = \arctan\left(\frac{p_1(y)}{p_1(x)}\right) \tag{2.23}$$

and is defined positive counterclockwise (ccw) from the positive x-axis.

Note that azimuth estimates should be interpreted in combination with rectilinearity and dip. In addition to the importance of high rectilinearity, it provides highest reliability if the particle motion on the horizontal components is significant, i.e., if the dip is not too steep (compare Figure 2.7 (a) and (c)). Therefore a measure for the azimuth reliability can be obtained using the rectilinearity value L and a weighting factor inversely proportional to the steepness of the dip:

$$\mathcal{R} = L \cdot \cos\phi. \tag{2.24}$$

The interpretation of the obtained orientation results needs to be done carefully. The results for P-waves are directly indicate the direction towards the source independent whether it was an explosion source or a double couple source because the particle motion occurs in propagation direction. In contrast, the dip and azimuths obtained from S-waves are not directly invertible in terms of the source directions. Some effects can be seen looking at synthetic data modeled in a homogeneous isotropic media using a double couple source in the x-z plane. The equations used for modeling are given in section 2.2. The radiation pattern from such a source can be expressed in terms of P-wave radiation as well as SH-wave and SV-wave radiation as shown in Figure 2.5.

For a source at $x = 0$ m, $y = 0$ m and $z = 2100$ m (see Figure 2.8 and Table 2.1) and receivers in two vertical monitoring wells, (#1 at x =35 m, y =300 m and #2 at x = 350 m, y =250 m), synthetic data as shown in Figure 2.9 (a) can be modeled (some white and isotropic noise was also added to the data). For both vertical arrays the lowermost receiver was located at a smaller depth as the source. Rectilinearities, dips and azimuths are calculated using a moving time window of
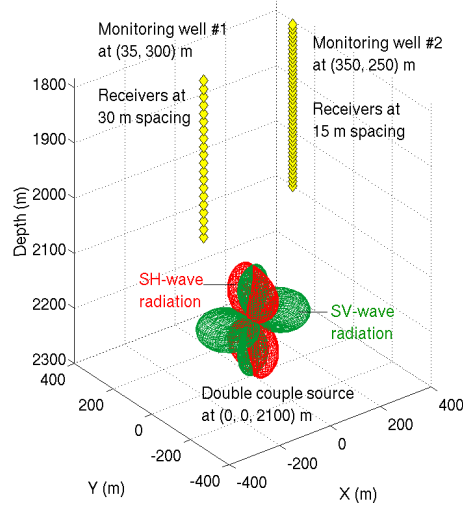
Figure 2.8: Aquisition geometry for synthetic data radiated from a double couple source in the center of the model. The radiation pattern of the S-waves is color-coded: green for SV-waves and red for SH-waves.

	x (m)	y (m)	z (m)	additional information
Example 1				
Source	0	0	2100	Double couple in the x-z plane
Monitoring well #1	35	300	1380-1950	20 receivers at 30 m spacing
Monitoring well #2	350	250	1265-1850	40 receivers at 15 m spacing
				$v_P = 5300$ m/s, $v_S = 3060$ m/s
Example 2				
Source 1 (E1)	50	100	3000	Double couple in the x-z plane
Source 2 (E2)	50	50	2100	Double couple in the x-z plane
				50 ms delay between events
Monitoring well #1	350	20	2250-2850	20 receivers at 30 m spacing
Monitoring well #2	250	350	2350-2935	40 receivers at 15 m spacing
				$v_P = 5300$ m/s, $v_S = 3060$ m/s

Table 2.1: Parameter for the synthetic data analyzed in this section.

20 ms length. The rectilinearity versus time plot in Figure 2.9 (b) clearly separates the linearly polarized body waves from the background noise. Later in this work a P-wave detection algorithm will be presented that makes use of this separation possibility.

The resulting dips and azimuths versus time are shown in Figure 2.9 (c) and (d). The dips observed for the P-waves are very consistent and increase the higher the receivers are located in the monitoring wells. The azimuths of the P-waves also reflect remarkably the source receiver geometry. For this reason the P-wave dips and azimuths can be used to invert for the source direction. The S-wave recorded in monitoring well #1 shows almost zero dip over the whole array. This is consistent with what we should observe since Figure 2.8 indicates that mainly SH-waves will be observed at vertical arrays located close to the y-axis. The azimuth calculated from this SH-wave shows a 90 degree offset to the P-wave azimuth. As shown in equation (2.23) the azimuth is calculated using only the horizontal components of the largest eigenvector. Whether the azimuth can be inverted for the source azimuth by adding 90 degree depends on the following condition:

$$\mathbf{r} \cdot \mathbf{S} = r_x s_x + r_y s_y = 0, \tag{2.25}$$

where $\mathbf{r}$ is the direction vector towards the source and $\mathbf{S}$ the S-wave particle motion vector (the largest eigenvector, respectively). Per definition the S-wave particle motion vector is perpendicular to the propagation direction which means $\mathbf{r} \cdot \mathbf{S} = r_x s_x + r_y s_y + r_z s_z = 0$. Hence the condition in equation (2.25) is only fulfilled if $r_z = 0$ or $s_z = 0$, which is the case for SH-waves or if the receiver is at the same depth as the source.

Consequently, the S-wave azimuths obtained in monitoring well #1 could be used to invert for the source azimuth. In contrast, the azimuths in monitoring well #2 (see Figure 2.9 (c) and (d)) do not fulfill the condition given in equation (2.25) or at least not over the full length of the array. The azimuth varies over the 600 m array (15 m spacing $\times$ 40 receiver) from almost 0 to 90 degree which is a result of the recording geometry and the SV-wave radiation pattern. Hence, the source azimuth cannot be inverted from the S-wave azimuths in monitoring well #2.

It is clear that the interference of different phase arrivals, e.g., from a second event, influences the polarization estimates. In Figure 2.10 (a) synthetic data are shown which demonstrate the effects of arrival interference. The data were modeled with two double couple sources and the recording network consisted of two monitoring wells. Monitoring well #1 is placed at $x = 350$ m and $y = 20$ m and well #2 at $x = 350$ m, $y = 250$ m. Where the phase arrivals intersect, the resulting particle motion estimate is a combination of the particle motion vectors of the individual arrivals. Depending on the individual wave types it may even result in high rectilinearity values as shown in Figure 2.10 (b) where the P-wave of the second event E2 intersects the S-wave of the first event E1 in monitoring well #1 or where the
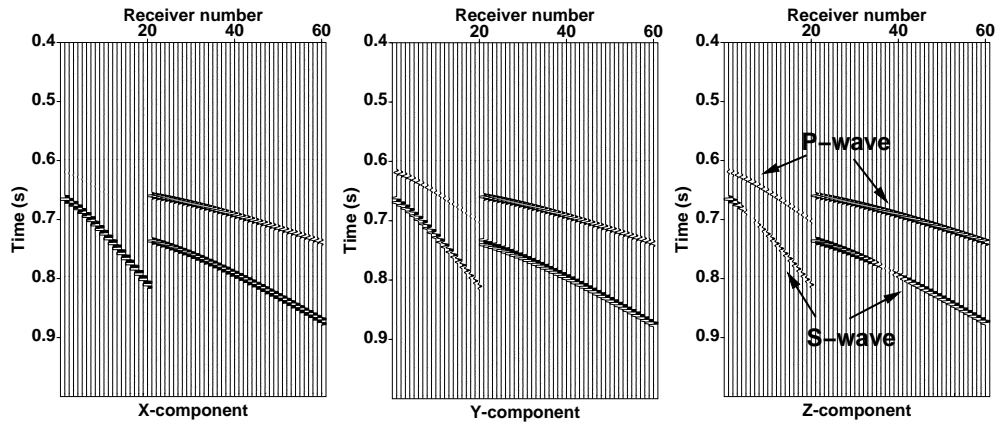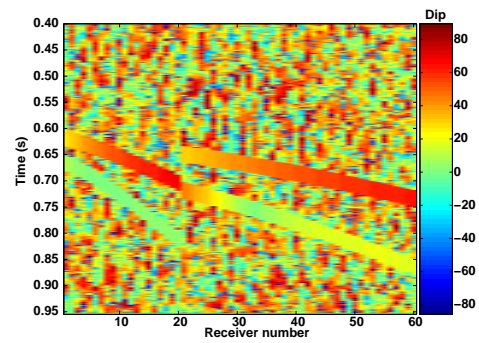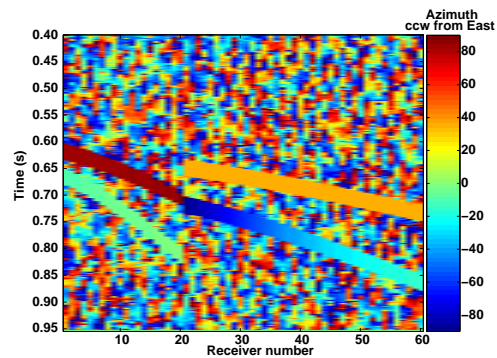
(a) Three-component seismograms.
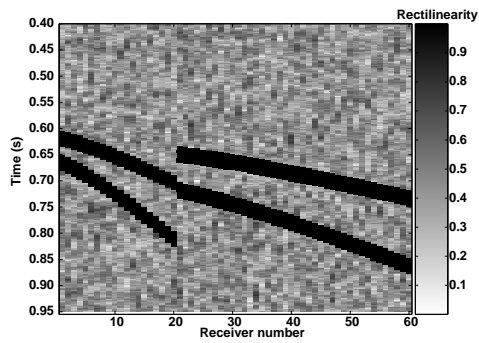
(b) Rectilinearity.
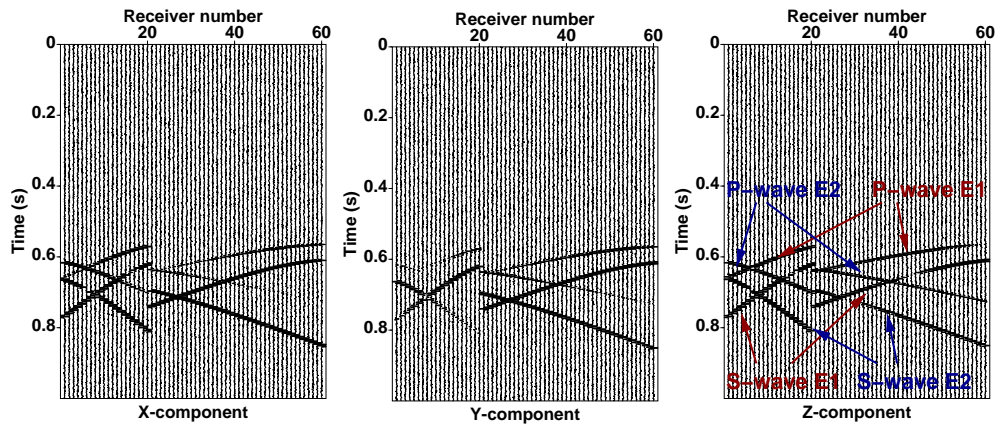

(c) Dip.

(d) Azimuth.

Figure 2.9: Polarization analysis of synthetic data generated using a double couple source in the x-z-plane for a homogeneous isotropic medium. The radiation pattern of this source is shown in Figure 2.5 and 2.8. The monitoring network consists of two vertical wells (see Table 2.1, Parameters for Example 1)). The first 20 receivers correspond to monitoring well #1 and the other 40 receivers to a monitoring well #2, respectively.

S-wave of E1 intersects both the P- and S-wave of E2. In the case shown here only the P-wave interference of E1 and E2 in well #2 shows a small but recognizable rectilinearity decrease. The dip and azimuth estimation also demonstrates that the orientation of a dominating arrival may be preserved (see e.g. Figure 2.10 (c) and (d) in well #2 where the S-wave of E1 intersects with the P-wave of E2). Both, azimuth and dip of the S-wave of E1 are still consistent with the estimates of neighboring receivers that are not effected by arrival interference. Hence a consistency check comparing the estimated dip and azimuth with estimates from other receivers in an array can provide useful information about the reliability of the estimated value. Here, such a test would show that the P-wave of E2 has inconsistent polarization for receivers 35 - 41, whereas the estimates for the S-wave polarization of E1 was preserved at these receivers.

It is intuitive that the length of the investigated time interval influences the resulting polarization parameters. In fact, the interval length influences resolution and stability. Polarization parameters obtained from a very long interval may become very smooth and consequently the resolution decreases. It can also lead to wrong estimates, especially when the interval contains more than one phase arrival. The effects would be the same as for intersecting phase arrivals which was discussed above. On the other hand, polarization parameters obtained from a too short interval may be unstable while resolving the instantaneous polarization attributes very good. The most extreme interval length - one sample long - was proposed by Li and Crampin (1991). Of course, the parameter of rectilinearity is meaningless when only one time sample is considered. Instantaneous azimuth and dip can be estimated but may become highly variable depending on the signal-to-noise ratio of the considered data. Nevertheless, a sample-by-sample estimate of polarization orientation can resolve orientations of partly intersecting arrivals and is less computationally expensive than the covariance matrix based estimate.

In this thesis, both instantaneous as well as interval-approximated polarization estimates will be used for the location of seismic sources. For the interval-approximated polarization estimates time intervals of the length of one or two dominant signal periods are used since this provides the best compromise between stability and resolution. Furthermore, the investigations of polarization attributes have shown that P-wave polarization attributes are directly invertible with respect to propagation directions whereas S-wave polarizations need careful interpretations. For this reason, the use of the P-wave polarization for seismic source location was chosen over the use of S-wave polarization even if the S-wave might provide a more dominant signal.
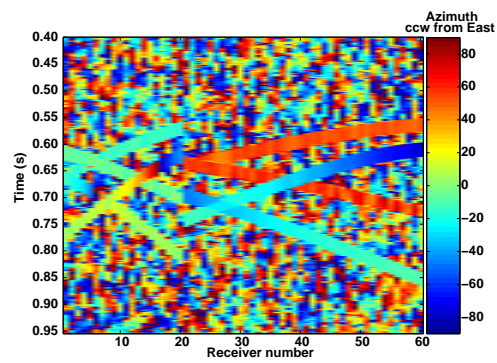
(a) Three-component seismograms.
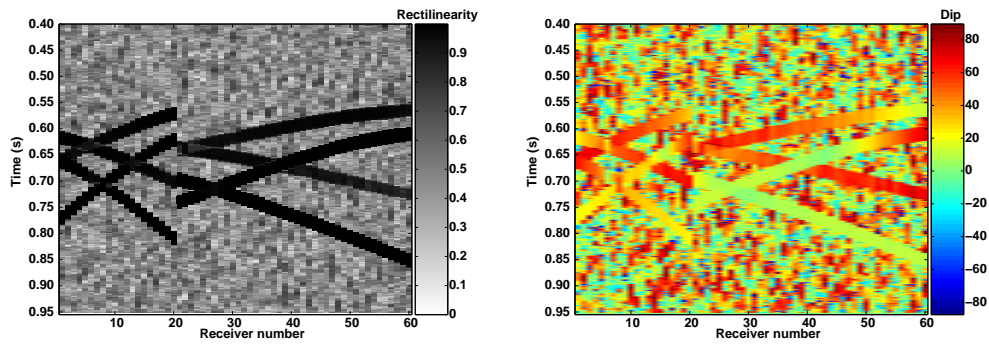
(b) Rectilinearity.

(c) Dip.

(d) Azimuth.

Figure 2.10: Polarization analysis of synthetic data generated using two double couple sources in an homogeneous isotropic medium. The monitoring network consists of two vertical wells (see Table 2.1, Parameters for Example 2)). The first 20 receivers correspond to monitoring well #1 and the other 40 receivers to a monitoring well #2, respectively.

2.4 Ray Theory

Seismic signals in complex media are difficult to describe and it takes a lot of computational power to simulate realistic wave propagation. Much less computational power is needed to approximate the propagation of body-waves with raytracing. In literature ray theory is intensively discussed and a complete description and derivation can be found in the books of Červený (2001) and Chapman (2004). The approach is based on an asymptotic high frequency approximation to the wave equation and commonly used for several applications such as reflection seismics, refraction seismics or seismology. The high frequency approximation means that the wavelength is small compared with the propagation distances and the spatial variations / heterogeneities of the medium. These circumstances may require smoothing of input models but also allow us to consider the propagating wave locally as a plane wave.

When talking about raytracing it is necessary to distinguish between kinematic ray tracing and dynamic ray tracing. The kinematic ray theory describes the geometry and times of rays and wavefronts whereas dynamic raytracing considers geometrical spreading of rays and the magnitude of the displacement.

In this thesis only kinematic ray tracing is considered since for the location method mainly the geometry and times of rays are needed. The description of the acoustic kinematic ray theory starts with the equation of motion

$$\frac{\partial \mathbf{v}}{\partial t} = -\frac{1}{\rho}\nabla P + \frac{1}{\rho}f \tag{2.26}$$

and its constitutive relation

$$\frac{\partial P}{\partial t} = -\kappa \nabla \cdot \mathbf{v}. \tag{2.27}$$

Here $\mathbf{v}$ describes the velocity of the medium (particle velocity), P the pressure, ρ the density, κ the bulk modulus and t represents the time. The symmetry of these equations implies that velocity and pressure have similar solutions. Chapman (2004) uses the following ansatz to solve the equations:

$$\mathbf{v}(\omega, \mathbf{x}_R) = f(\omega) \sum_n e^{i\omega T(\mathbf{x}_R, \mathcal{L}_n)} \sum_{m=0}^{\infty} \frac{\mathbf{v}^{(m)}(\mathbf{x}_R, \mathcal{L}_n)}{(-i\omega)^m} \tag{2.28}$$

and

$$-P(\omega, \mathbf{x}_R) = f(\omega) \sum_n e^{i\omega T(\mathbf{x}_R, \mathcal{L}_n)} \sum_{m=0}^{\infty} \frac{-P^{(m)}(\mathbf{x}_R, \mathcal{L}_n)}{(-i\omega)^m}. \qquad (2.29)$$

The ansatz is written in the frequency (ω) domain and $f(\omega)$ is an arbitrary spectrum depending on the source. The notation $\mathcal{L}_n$ and the corresponding summation over n is used by Chapman (2004) to indicate that more than one path may exist from a source point to the point $\mathbf{x}_R$ which is known as ray expansion. T represents the travel-time function, and $^{(m)}$ denotes the index, whereas $(...)^m$ refers to the power of m. In homogeneous media acoustic and elastic waves propagate approximately without dispersion with a frequency-independent velocity and satisfy Snell's law at interfaces. In inhomogeneous media similar behavior can be observed as long as the wavelength is small compared to the spatial variation. Therefore Chapman (2004) writes his ansatz as a series in amplitude coefficients $\mathbf{v}^{(m)}$ and $P^{(m)}$.

Substituting equation (2.28) and (2.29) into equation (2.26) (without the body force term) leads to:

$$f(\omega) \sum_n i\omega \cdot e^{i\omega T(\mathbf{x}_R, \mathcal{L}_n)} \sum_{m=0}^{\infty} \frac{\mathbf{v}^{(m)}(\mathbf{x}_R, \mathcal{L}_n)}{(-i\omega)^m} =$$
$$\frac{-1}{\rho} \cdot \left(f(\omega) \sum_n i\omega \cdot e^{i\omega T(\mathbf{x}_R, \mathcal{L}_n)} \cdot \nabla T(\mathbf{x}_R, \mathcal{L}_n) \sum_{m=0}^{\infty} \frac{-P^{(m)}(\mathbf{x}_R, \mathcal{L}_n)}{(-i\omega)^m} \right)$$
$$- \frac{1}{\rho} \cdot \left(f(\omega) \sum_n e^{i\omega T(\mathbf{x}_R, \mathcal{L}_n)} \sum_{m=0}^{\infty} \frac{-\nabla P^{(m)}(\mathbf{x}_R, \mathcal{L}_n)}{(-i\omega)^m} \right) \quad (2.30)$$

and into equation (2.27)

$$f(\omega) \sum_n i\omega \cdot e^{i\omega T(\mathbf{x}_R, \mathcal{L}_n)} \sum_{m=0}^{\infty} \frac{-P^{(m)}(\mathbf{x}_R, \mathcal{L}_n)}{(-i\omega)^m} =$$
$$- \kappa \cdot \left(f(\omega) \sum_n i\omega \cdot e^{i\omega T(\mathbf{x}_R, \mathcal{L}_n)} \cdot \nabla T(\mathbf{x}_R, \mathcal{L}_n) \sum_{m=0}^{\infty} \frac{\mathbf{v}^{(m)}(\mathbf{x}_R, \mathcal{L}_n)}{(-i\omega)^m} \right)$$
$$- \kappa \cdot \left(f(\omega) \sum_n e^{i\omega T(\mathbf{x}_R, \mathcal{L}_n)} \sum_{m=0}^{\infty} \frac{\nabla \cdot \mathbf{v}^{(m)}(\mathbf{x}_R, \mathcal{L}_n)}{(-i\omega)^m} \right), \quad (2.31)$$

respectively. Omitting the argument $(\mathbf{x}_R, \mathcal{L}_n)$ and defining boundary conditions ($\mathbf{v}^{(-1)} = 0$ and $P^{(-1)} = 0$) equation (2.30) and equation (2.31) can be written as

$$\rho \sum_{m=0}^{\infty} \frac{\mathbf{v}^{(m)}}{(-i\omega)^m} = -\nabla T \sum_{m=0}^{\infty} \frac{-P^{(m)}}{(-i\omega)^m} + \sum_{m=0}^{\infty} \frac{-\nabla P^{(m-1)}}{(-i\omega)^m} \qquad (2.32)$$

$$\sum_{m=0}^{\infty} \frac{P^{(m)}}{(-i\omega)^m} = \kappa \cdot \left(\nabla T \sum_{m=0}^{\infty} \frac{\mathbf{v}^{(m)}}{(-i\omega)^m} - \sum_{m=0}^{\infty} \frac{\nabla \mathbf{v}^{(m-1)}}{(-i\omega)^m} \right). \qquad (2.33)$$

The coefficients of each power of ω are set zero (as they must be to make the equation valid for arbitrary frequency) and it follows

$$-\nabla P^{(m-1)} = \rho \mathbf{v}^m - \mathbf{p} P^m \qquad (2.34)$$

$$\kappa \nabla \cdot \mathbf{v}^{(m-1)} = \kappa \mathbf{p} \cdot \mathbf{v}^m - P^m \qquad (2.35)$$

for $m \geq 0$, with the slowness vector

$$\mathbf{p} = \nabla T. \qquad (2.36)$$

The next step is to eliminate $\mathbf{v}^m$ from equation (2.34) which can be done by rearranging equation (2.35) and substituting it into equation (2.34):

$$-\nabla P^{(m-1)} = \rho \frac{\kappa \nabla \cdot \mathbf{v}^{(m-1)} + P^{(m)}}{\kappa \mathbf{p}} - \mathbf{p} P^m$$

$$(\kappa \mathbf{p}^2 - \rho) P^{(m)} = \kappa \left(\mathbf{p} \cdot \nabla P^{(m-1)} + \rho \nabla \cdot \mathbf{v}^{(m-1)} \right) \qquad (2.37)$$

For $m = 0$ and using again the boundary conditions ($\mathbf{v}^{(-1)} = 0$ and $P^{(-1)} = 0$) this equation reduces to :

$$\left(\frac{\kappa}{\rho} \mathbf{p}^2 - 1 \right) P^{(0)} = \left(\alpha^2 \mathbf{p}^2 - 1 \right) P^{(0)} = 0, \qquad \text{with} \qquad \sqrt{\frac{\kappa}{\rho}} = \alpha. \qquad (2.38)$$

The series of amplitude coefficients in the ansatz (2.29) can always be defined in a way that $m = 0$ holds the first non-zero term and hence the coefficient $P^{(0)}$ can be assumed to be non-zero. Therefore it is possible to rewrite equation (2.38):

$$(\nabla T)^2 = \frac{1}{\alpha^2} \qquad (2.39)$$
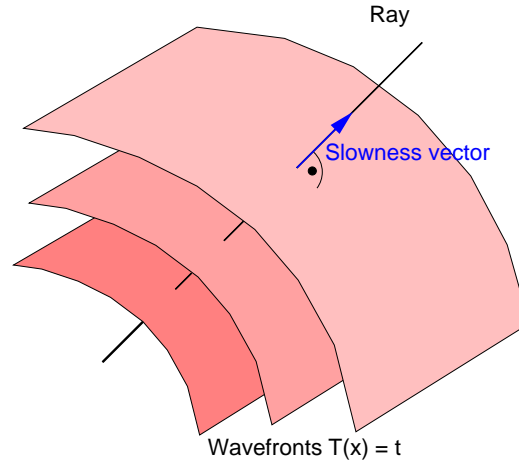
2.4. Ray Theory

Figure 2.11: The ray path must be in the direction of the slowness vector and orthogonal to the wavefronts.

which is known as the eikonal equation. Wavefronts are the surfaces where the travel-time function is $T(\mathbf{x}) = t$. The slowness vector is perpendicular to the wavefronts as shown in Figure 2.11. The ray is defined as the trajectory orthogonal to the wavefronts which can be parameterized in arc length s. Assuming s increases with increasing T the eikonal equation becomes:

$$\frac{dT}{ds} = \frac{1}{\alpha} \tag{2.40}$$

Under these circumstances the ray path $d\mathbf{x}/dT$ must be in the direction of the slowness vector and from equation (2.40) it follows (with $|d\mathbf{x}| = ds$)

$$\frac{d\mathbf{x}}{dT} = \alpha^2 \mathbf{p}. \tag{2.41}$$

Using equation (2.40) and (2.36) the change of the slowness vector is

$$\frac{d\mathbf{p}}{dT} = -\frac{\nabla \alpha}{\alpha}. \tag{2.42}$$

Equation (2.41) and (2.42) represent the kinematic ray equations. Since the location method presented in this work will use initial conditions (values) for the position $\mathbf{x}_0$ and the direction $\mathbf{p}_0$ the ray path can be obtained solving these differential equations. In many scientific applications the fourth-order-Runge-Kutta (RK4) method is used to numerically integrate ordinary differential equations (Press et al., 1992). This approach evaluates the derivatives once at the beginning of the interval (initial point) k_1, twice at midpoints k_2 and k_3, and once at the end of the interval k_4:

$$
\begin{aligned}
k_1 &= \Delta t f(x_n, y_n) \\
k_2 &= \Delta t f(x_n + \frac{1}{2}\Delta t, y_n + \frac{1}{2}k_1) \\
k_3 &= \Delta t f(x_n + \frac{1}{2}\Delta t, y_n + \frac{1}{2}k_2) \\
k_4 &= \Delta t f(x_n + \Delta t, y_n + k_3)
\end{aligned}
$$

(2.43)

(2.44)

Then the new increment $y_{(n+1)}$ is calculated as a weighted average of these estimated increments

$$
y_{(n+1)} = y_n + \frac{1}{6}k_1 + \frac{2}{6}k_2 + \frac{2}{6}k_3 + \frac{1}{6}k_4 + O(\Delta t^5)
\tag{2.45}
$$

where k_2 and k_3, the two midpoint values, give double weights. This method is reasonably simple and robust and provides a stable and accurate numerical solution of differential equations as long as the propagation increment - here a ray tracing time step Δt - is sufficiently small compared to the variations in the integration interval. The RK4 method has an error that is proportional to Δt^5 for an integration step, while the total accumulated error is proportional to Δt^4.

Hence, the time step for the ray propagation needs to be chosen carefully. On the other hand, the use of small propagation time steps increases the number of time steps necessary to trace a ray of a fixed length, which may result in an unreasonable long computation time. Press et al. (1992) recommends the use of adaptive step size control to achieve some predetermined accuracy in the solution with minimum computational effort. However, in this work the number of rays as well as the considered length of rays was expected to be reasonable small and the adaptive step size control was not implemented in the ray tracing method.